coatings

MDPI

Article

On the Analysis of the Non-Newtonian Fluid Flow Past a Stretching/Shrinking Permeable Surface with Heat and Mass Transfer

Shahid Khan [1], Mahmoud M. Selim [2,3], Aziz Khan [4], Asad Ullah [5], Thabet Abdeljawad [4,6,7,*], Ikramullah [8], Muhammad Ayaz [9] and Wali Khan Mashwani [1]

[1] Institute of Numerical Sciences, Kohat University of Science & Technology, Kohat 26000, Khyber Pakhtunkhwa, Pakistan; shahidkhan@kust.edu.pk (S.K.); mashwanigr8@gmail.com (W.K.M.)
[2] Department of Mathematics, Al-Aflaj College of Science and Humanities Studies, Prince Sattam Bin Abdulaziz University, Al-Aflaj 710-11912, Saudi Arabia; m.selim@psau.edu.sa
[3] Department of Mathematics, Suez Faculty of Science, Suez University, Suez 34891, Egypt
[4] Department of Mathematics and General Sciences, Prince Sultan University, P.O. Box 66833, Riyadh 11586, Saudi Arabia; akhan@psu.edu.sa
[5] Department of Mathematical Sciences, The University of Lakki Marwat, Lakki Marwat 28420, Khyber Pakhtunkhwa, Pakistan; asad@ulm.edu.pk
[6] Department of Medical Research, China Medical University, Taichung 40402, Taiwan
[7] Department of Computer Science and Information Engineering, Asia University, Taichung 40402, Taiwan
[8] Department of Physics, Kohat University of Science & Technology, Kohat 26000, Khyber Pakhtunkhwa, Pakistan; ikramullah@kust.edu.pk
[9] Department of Mathematics, Abdul Wali Khan University, Mardan 23200, Khyber Pakhtunkhwa, Pakistan; mayazmath@awkum.edu.pk
* Correspondence: tabdeljawad@psu.edu.sa

Citation: Khan, S.; Selim, M.M; Khan, A.; Ullah, A.; Abdeljawad. T.; Ikramullah; Ayaz. M.; Mashwani, W.K. On the Analysis of the Non-Newtonian Fluid Flow Past a Stretching/Shrinking Permeable Surface with Heat and Mass Transfer. *Coatings* **2021**, *11*, 566. https://doi.org/10.3390/coatings11050566

Academic Editor: Eduardo Guzmán

Received: 4 April 2021
Accepted: 29 April 2021
Published: 12 May 2021

Abstract: The 3D Carreau fluid flow through a porous and stretching (shrinking) sheet is examined analytically by taking into account the effects of mass transfer, thermal radiation, and Hall current. The model equations, which consist of coupled partial differential equations (PDEs), are simplified to ordinary differential equations (ODEs) through appropriate similarity relations. The analytical procedure of HAM (homotopy analysis method) is employed to solve the coupled set of ODEs. The functional dependence of the hydromagnetic 3D Carreau fluid flow on the pertinent parameters are displayed through various plots. It is found that the x-component of velocity gradient ($f^{'}(\eta)$) enhances with the higher values of the Hall and shrinking parameters (m, ϱ), while it reduces with magnetic parameter and Weissenberg number (M, We). The y-component of fluid velocity ($g(\eta)$) rises with the augmenting values of m and M, while it drops with the augmenting viscous nature of the Carreau fluid associated with the varying Weissenberg number. The fluid temperature $\theta(\eta)$ enhances with the increasing values of radiation parameter (Rd) and Dufour number (Du), while it drops with the rising Prandtl number (Pr). The concentration field ($\phi(\eta)$) augments with the rising Soret number (Sr) while drops with the augmenting Schmidt number (Sc). The variation of the skin friction coefficients (C_{fx} and C_{fz}), Nusselt number (Nu_x) and Sherwood number (Sh_x) with changing values of these governing parameters are described through different tables. The present and previous published results agreement validates the applied analytical procedure.

Keywords: thermal radiations; magnetic field; Carreau fluid; stretching/shrinking surface; Hall effect; nonlinear radiations; HAM

1. Introduction

The thermal energy transportation and the fluid boundary layer motion over stretching (shrinking) sheets are the areas of immense importance due to its broad range industrial and technological applications. Some of the applications consist of: growing crystals structures,

plastic sheets preparation, manufacturing of electronic chips and materials, paper industry, cooling process, and so on [1,2]. The basic work in this regard was started by Crane [3]. Andersson et al. [4], and Vajravelu [5] discussed the different aspects of fluids flowing over stretching surfaces. It is important to mention here that the gradients' existence are essential for the growth of various fluxes and flows. In fluids, there are two important effects named as Soret and Dufor effects. In Soret effect, the existence of temperature gradient results in thermal diffusion which governs the thermal energy flow. The mass transfer is mainly governed by Dufor effect, which gives rise to the diffusion-thermo effect. These effects have an influential role in governing the natural convective flow, which is one of the modes by which thermal energy can transfer due to the aggregate motion of the heated fluid. The term cross diffusion refers to the process in which the existence of concentration gradient of one specie develops the flux of the other. This means that the cross diffusion is associated with both thermal and mass diffusion. The heat energy exchangers, steel processing, cooling of nuclear power plant, etc. are the well-known technological sectors in which the convection thermal energy transportation plays an important role. The different aspects during the heat energy flow over a 3D exponentially stretching surface are investigated by Liu et al. [6]. Hayat et al. [7] examined the boundary layer Carreau fluid motion and obtained that the presence of suction depreciates (enhances) the Carreau fluid speed (boundary layer thickness). Further detail analysis about the boundary layer flow can be accessed in refs [8–10].

The Magneto-Hydro-dynamics (MHD) studies the evolution of the macroscopic behaviors of fluids in the ambient magnetic field presence. The MHD flow finds its applications in Astrophysics and Astronomy, nuclear reactors cooling, engineering and technology, Plasma Physics, etc. Nazar et al. [11] investigated the thermal energy transformation during the magnetized flow over a vertical and stretchable surface. During their investigation, they found that the enhancing B-field magnitude reduces the coefficient of skin friction and the thermal energy loss. The analytic investigation of heat energy transfer during the 3D MHD migration over a stretchable plate is carried out by Xu et al. [12] using the series solution approach. The MHD stagnation flow toward an extendable surface is examined by Ishak et al. [13]. A more recent study on stagnation point flow can be found in references [14,15]. The heat energy transfer through convection during the magnetized 3D motion on an extendable surface is worked out by Vajravelu et al. [16]. Pop and Na [17] examined the impacts of B-field on the fluid flowing through a porous and stretchable surface. The recent developments on the magnetized boundary-layer motion can be found in references [18–21].

The thermal energy radiations and its analysis are extremely important in the solar energy, fission reactors, engines, propulsion equipment for speedy aircrafts, and various chemical phenomena operating at extreme temperatures. Gnaneswara Reddy [22] studied the magnetized nanofluid motion by incorporating the impact of thermal energy radiation. The mixed convection MHD fluid flow through a perforated enclosure is examined by Gnaneswara Reddy [23]. He investigated the effects produced due to chemical reaction, Ohmic dissipation, and heat energy source. Emad [24] investigated the different impacts that arose due to the inclusion of thermal radiations in a conducting fluid flow. The influence of thermal radiations on the thermal energy transfer through convection in an electrically conducting fluid of varying viscosity moving over an extending surface is worked out by Abo-Eldahab and Elgendy [25]. Gnaneswara Reddy [26] investigated the various impacts arose due to Joule-heating, thermo-phoresis and viscous nature of a magnetized fluid flowing over an isothermal, perforated and inclined surface. A more recent and detailed investigation of the MHD flow can be found in references [27–30]. Yulin et al. [31] numerically studied the natural convection flow of nanofluid over inclined enclosure. They investigated the different impacts due to constant heat energy source and temperature. Zhe et al. [32] performed an experimental analysis of water, ethylene glycol, and copper oxides mixture by employing statistical techniques for the multi-walled-carbon-nanotubes (MWCNTs). Shah et al. [33–35] analytically scrutinized the micropolar fluid

in different frames. Hayat et al. [36] analyzed the Cu-water MHD nanofluids flow in the rotating disks. Dat et al. [37] have recently studied numerically the $\gamma-$AlOOH nanoliquid by using different shaped nanoparticles within a wavy container. The recent studies about the nanaofluids along with different advantages can be studied in refs. [38–46].

Fluids are categorized broadly as non-Newtonian and Newtonian. The Newton viscosity relation which shows that the shear stress and strain are directly related, is applicable in the Newtonian fluid. The non-Newtonian fluid can not be described by this simple direct relation between stress and strain. The non-Newtonian fluids, for example manufactured and genetic liquid organisms, blood, polymers, liquids, etc., have central importance in this advance technological world. The non-Newtonian fluids are very hard to be analytically and numerically treated, as compared to the Newtonian fluids, due to its nonlinear behavior. The credit goes to Carreau [47], who developed a relation that describes both, the viscoelastic and nonlinear properties of of such type of complex fluids. Ali and Hayat [48] worked out the Carreau fluid peristaltic motion through an asymmetrical enclosure. Goodarzi et al. [49] analyzed the simultaneous impact of slip and temperature jump over the Non-Newtoinian nanofluid (alumina + carboxy-methyl cellulose) motion through microtube, and investigated the impacts of pertinent parameters over the nanofluid state variables. Maleki et al. [50] analyzed the impacts of heat generation (absorption), suction (injection), nanoparticles type (volume fraction), thermal and velocity slip parameter, and radiation on the temperature and velocity fields of four different types of nanofluids moving over a perforated flat surface. Hayat et al. [51] studied the impacts of induced magnetic field on the flow of Carreau fluid. Tshehla [52] examined the Carreau fluid migration past an inclined surface. Elahi et al. [53] analyzed the Carreau fluid 3D migration from a duct. Gnaneswara Reddy et al. [54] studied the effects due to Ohmic heating during the MHD viscous nanofluid motion through a nonlinear, permeable, and extending surface. Jiaqiang et al. [55] employed the wetting models in order to explain the working procedures of different surfaces found in nature. Khan et al. [56,57] employed the fractional model to Casson and Brinkman types fluids. The impacts produced due to the incorporation of thermal radiations in the presence of suction (injection) on the MHD flow of fluids are investigated by researchers [58–60]. Maleki et al. [61] analyzed the impact of heat generation (absorption) and viscous dissipation on the heat transfer during the non-Newtonian pseudoplastic nanomaterial motion over a perforated flate. Gheynani et al. [62] examined the turbulent motion of a non-Newtonian Carboxymethyl cellulose copper oxide nanofluid in a 3D microtube by investigating the impacts of nanoparticle concentration and diameter over the temperature and velocity fields. Maleki et al. [63] studied the heat transfer characteristics of pseudo-plastic non-Newtonian nanofluid motion over a permeable surface in the presence of suction and injection. The system of governing PDEs is converted to ODEs by using similarity solution technique, and then solved numerically by employing Runge–Kutta–Fehlberg fourth–fifth order (RKF45) method. The numerical investigation of (water + alumina) nanofluid mixed flow through a 2D square cavity having porous medium is carried out by Nazari et al. [64] employing a Fortran Code.

The phenomenon in which the application of an external magnetic-field to a conducting fluid produces potential difference, is termed the Hall effect. The impacts due to the inclusion of Hall effect are examined by various researchers due to its relevance with a variety of technological and industrial applications. Biswal and Sahoo [65] investigated the impacts of Hall current on the magnetized fluid motion over a vertical, permeable and oscillating surface. Raju et al. [66] worked out the Hall current impacts on the MHD flow over an oscillatory surface having porous upper wall. Datta and Janna [67] analyzed the magnetized and oscillatory fluid motion on a flat surface in the presence of Hall current. Aboeldahab and Elbarbary [68] analyzed the impacts due to Hall current during the MHD fluid dynamics through a semi-infinite and perpendicular plate. Khan et al. [69] used the finite element method for the Newtonian fluid past a semi-circular cylinder. The variation in temperature and mass diffusion in the MHD fluid flow considering the inclusion of Hall

effect is examined by Rajput and Kanaujia [70]. Further studies on similar footings are performed by Shah et al. [71–73] employing semi-analytical calculations. The magnetized and peristaltic fluid dynamics of Carreau–Yasuda fluid through a channel is numerically investigated by Abbasi et al. [74] taking into account the Hall effect impact. Abdeljawad et al. [74] investigated the 3D magnetite Carreau fluid migration through a surface of parboloid of revolution by incorporating mass transfer and thermal radiations. The impacts of Hall current and cross diffusion on the two dimensional (2D) MHD Carreau fluid flow through a perforated and stretchable (shrinkable) surface is recently investigated in [75].

Here, we extend the previous work [75] to 3-dimensional space in order to analyze what actually happens in the most general situation. The novelty of the current investigation is to examine analytically the thermal energy and mass transfer properties of the MHD Carreau fluid 3D motion through a perforated stretching sheet by considering the effects of Hall current and cross diffusion. This research work has potential applications in problems involving motion of the non-Newtonian fluid over perforated stretching (shrinking) surfaces. The research work carried out is organized in the following manner:

The geometrical description and model equations of the current investigation are presented in Section 2. The obtained results are discussed and explained by plotting various graphs in Section 3. The comparison and the computation of engineering-based related quantities are discussed through different tables in Section 4. The work is finally concluded in Section 5.

2. Mathematical Modeling

The 3D magnetized Carreau fluid is considered along a linear stretching and contracting permeable sheet by incorporating the impacts of thermal radiations and Hall current. The flow is assumed to be incompressible, laminar, steady, and electrically conducting. The external magnetic field B_0 is applied in the y-direction. The thermal energy and mass diffusion impacts due to the existence of temperature gradient and concentration gradient are considered as well. The geometry is chosen in such a way that the sheet velocities along x-and $y-$axis are respectively u_w and v_w, whereas the flow is restricted to the positive $z-$axis, as can be seen in Figure 1. Furthermore, convective heat energy flow and mass transfer are considered on the sheet, such that the assumed liquid below the sheet has temperature T_f and concentration C_f in order to make them consistent with the heat and mass conversion coefficients h_1 and h_2.

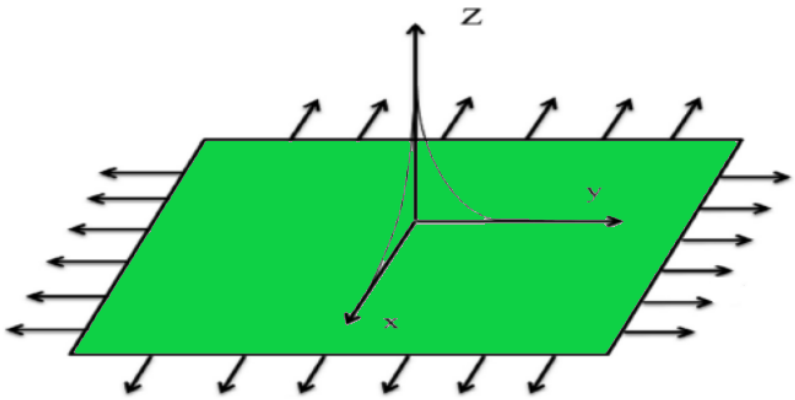

Figure 1. Geometrical description of the study.

The Carreau fluid flow is governed by the relation [47,76]:

$$\eta = \left[\eta_\infty + (\eta_0 - \eta_\infty)\left(1 + (\lambda\dot{\gamma})^2\right)^{\frac{n-1}{2}}\right], \quad (1)$$

where η_0 (η_∞) denotes the zero (infinite) shear-rate viscosity, n is the index of power law, λ denotes the time constant of the material. The symbol $\dot{\gamma}$ is given by [76]:

$$\dot{\gamma} = \sqrt{\frac{1}{2}\sum_i\sum_j \dot{\gamma}_{ij}\dot{\gamma}_{ji}} = \sqrt{\frac{1}{2}\prod}, \tag{2}$$

where $\prod$ is the strain-rate tensor second invariant. Hall effect arises when magnetic field is applied externally to the conducting fluid which can modify the flow pattern. This phenomenon can be studied with the help of Ohm's law [75,77] given as:

$$\vec{j} + \frac{\omega_e t_e}{B_0} \times (\vec{j} \times \vec{B}) + \frac{\sigma P_e}{e n_e} = \sigma(\vec{V} \times \vec{B} + \vec{E}), \tag{3}$$

where $\vec{j}$ is the current density, ω_e (t_e) is the angular frequency (collision time interval) of electrons, σ denotes the conductivity, $\vec{E}$ ($\vec{B}$) is the electric field (magnetic field), n_e(e) is the number density (charge) of electrons, and P_e is the pressure of electrons. The $y-$component of $\vec{j}$ is zero due to the application of external magnetic field in this direction. The x and $z-$components of $\vec{j}$ are expressed in the chosen geometry as:

$$j_x = \frac{\sigma B_0^2 (mu - w)}{1 + m^2}, \tag{4}$$

$$j_z = \frac{\sigma B_0^2 (mw + u)}{1 + m^2}, \tag{5}$$

where $m = \omega_e t_e$ is the Hall parameter. Using Equations (1)–(5) at $\eta_\infty = 0$, the Carreau fluid equations are written respectively as [75]:

$$\frac{\partial u}{\partial x} + \frac{\partial v}{\partial y} + \frac{\partial w}{\partial z} = 0, \tag{6}$$

$$u\frac{\partial u}{\partial x} + v\frac{\partial u}{\partial y} + w\frac{\partial u}{\partial z} - \nu\frac{\partial^2 u}{\partial y^2}\left(1 + \left(\frac{n-1}{2}\right)\lambda^2\left(\frac{\partial u}{\partial y}\right)^2\right) = \nu(n-1)\lambda^2\frac{\partial^2 u}{\partial y^2}(\frac{\partial u}{\partial y})^2 \times \left(1 + (\frac{n-3}{2})\lambda^2(\frac{\partial u}{\partial y})^2\right) - \frac{\sigma B_0^2(mw+u)}{\rho(1+m^2)} - \frac{\nu u}{k}, \tag{7}$$

$$u\frac{\partial w}{\partial x} + v\frac{\partial w}{\partial y} + w\frac{\partial w}{\partial z} - \nu\frac{\partial^2 w}{\partial y^2}\left(1 + \left(\frac{n-1}{2}\right)\lambda^2\left(\frac{\partial w}{\partial y}\right)^2\right) = \nu(n-1)\lambda^2\frac{\partial^2 w}{\partial y^2}(\frac{\partial w}{\partial y})^2 \times \left(1 + (\frac{n-3}{2})\lambda^2(\frac{\partial w}{\partial y})^2\right) + \frac{\sigma B_0^2(mu-w)}{\rho(1+m^2)} - \frac{\nu w}{k}, \tag{8}$$

$$u\frac{\partial T}{\partial x} + v\frac{\partial T}{\partial y} + w\frac{\partial T}{\partial z} = -\frac{1}{\rho c_p}\frac{\partial q_r}{\partial y} + \alpha\frac{\partial^2 T}{\partial y^2} + \frac{D_m K_T}{c_s c_p}\frac{\partial^2 C}{\partial y^2}, \tag{9}$$

$$u\frac{\partial C}{\partial x} + v\frac{\partial C}{\partial y} + w\frac{\partial C}{\partial z} = \frac{D_m K_T}{T_m}\frac{\partial^2 T}{\partial y^2} + D_m\frac{\partial^2 C}{\partial y^2}. \tag{10}$$

The system boundary restrictions are the following:

$$\begin{gathered} u = u_w(x) + L_1\frac{\partial u}{\partial y}, v = v_w, \frac{\partial T}{\partial y} = -\frac{h_1}{k}(T_f - T), \frac{\partial T}{\partial y} = -\frac{h_2}{D_m}(C_f - C), w = 0 \text{ at } y = 0, \\ u \to 0, w \to 0, T \to T_\infty, C \to C_\infty \text{ as } y \to \infty, \end{gathered} \tag{11}$$

where B_0 is the magnetic field magnitude, T (ρ) is the Carreau fluid temperature (density), k (c_s) is the Carreau fluid thermal conductivity (susceptibility of concentration), $u_w(x) = ax$ (v) is the fluid velocity x (y) component, K_T is the thermal diffusion ratio, C

is the concentration of the fluid, L_1 is the factor of the velocity slip, and D_m is the mass diffusivity. Furthermore, v_w is the mass flow velocity, and C_f (T_f) is the convective fluid concentration (temperature).

The flux of the radiations q_r is [75,78]:

$$\frac{\partial q_r}{\partial y} = -\frac{16\sigma^s T_0^3}{3k_1}\frac{\partial^2 T}{\partial y^2}, \tag{12}$$

where σ^s and k_1 are respectively the Stefan constant and average absorption coefficient. Applying Equation (12) to Equation (9), we will get the

$$u\frac{\partial T}{\partial x} + v\frac{\partial T}{\partial y} - \frac{D_m K_T}{c_s c_p}\frac{\partial^2 C}{\partial y^2} = \frac{\partial}{\partial y}\left[\left(\alpha + \frac{16\sigma^s}{3k_1}T_\infty^3\right)\frac{\partial T}{\partial y}\right]. \tag{13}$$

Using the similarity variables as below [75]:

$$\begin{gathered}\psi = \sqrt{av}f(\eta)x, \eta = \sqrt{\frac{a}{v}}y, T - T_\infty = (T_f - T_\infty)\theta(\eta), w = axg(\eta),\\ C - C_\infty = (C_f - C_\infty)\phi(\eta), T - T_\infty = T_\infty(\theta_w - 1)\theta, \theta_w = \frac{T_f}{T_\infty}.\end{gathered} \tag{14}$$

Here, a is constant. The symbols f, θ, and ϕ represent the non-dimensional fluid velocity, temperature, and concentration, respectively. The symbol ψ denotes the stream function satisfying $u = \frac{\partial \psi}{\partial y}$ and $v = -\frac{\partial \psi}{\partial x}$.

Applying these transformations in Equations (6), (7), (10), (13), and (14), we obtain

$$\begin{aligned}f'''\left[1 + \left(\frac{n-1}{2}\right)Wef''^2\right] + 2f'''\left[\left(\frac{n-1}{2}\right)Wef''^2\right]\left[1 + \left(\frac{n-3}{2}\right)Wef''^2\right]\\ + ff'' - f'^2 - \frac{M}{1+m^2}(f' + mg) - rf' = 0,\end{aligned} \tag{15}$$

$$\begin{aligned}g''\left[1 + \left(\frac{n-1}{2}\right)Weg'^2\right] + 2g''\left[\left(\frac{n-1}{2}\right)Weg'^2\right]\left[1 + \left(\frac{n-3}{2}\right)Weg'^2\right]\\ - gf' + g'f + \frac{M}{1+m^2}(mf' - g) + rg = 0,\end{aligned} \tag{16}$$

$$\theta''\left(1 + Rd(1 + (\theta_w - 1)\theta)^3\right) + \left(3(\theta_w - 1)\theta'^2(1 + \theta_w - 1)\theta)^2\right) + Prf\theta' + PrDu\phi'' = 0, \tag{17}$$

$$\phi'' + Scf\phi' + ScSr\theta'' = 0. \tag{18}$$

The boundary restrictions are transformed as:

$$\begin{gathered}f = \varrho, f' = 1 + \chi_1 f(0)'', g = 0, \theta' = -\chi_2(1 - \theta(0)), g = 0, \phi' = -\chi_3(1 - \phi(0)) \text{ at } \eta = 0,\\ f' \to 0, \theta \to 0, \phi \to 0, g \to 0 \quad \text{as} \quad \eta \to \infty.\end{gathered} \tag{19}$$

Here, the symbol We represents the Weissenberg number, ϱ shows the mass transfer parameter which describes suction ($\varrho > 0$) and injection ($\varrho < 0$). The symbol Rd denotes the radiation parameter, whereas Pr, Sc, and Du are respectively the Prandtl, Soret, and Dufour numbers. The symbols χ_2, χ_3 are the thermal and concentration profiles slip parameters, respectively. These parameters have the following definitions:

$$\begin{gathered}Sc = \frac{\nu}{D_m}, Pr = \frac{\nu}{a}, Rd = \frac{16\sigma * T_\infty^3}{3kk_e}, Du = \frac{D_m K_T(C_f - C_\infty)}{c_s c_p \nu(T_f - T_\infty)}, r = -\frac{-\nu}{ak},\\ We = \frac{\lambda^2 l^2 a^3}{\nu}, \chi_1 = L\sqrt{\frac{a}{v}}, \chi_2 = \frac{h_1}{k}\sqrt{\frac{a}{v}}, \chi_3 = \frac{h_2}{D_m}\sqrt{\frac{a}{v}}, \varrho = -\frac{v_w}{\sqrt{av}}, M = \frac{\sigma B_0^2}{\rho a}\end{gathered} \tag{20}$$

The basic physical quantities of engineering interest (Sherwood and Nusselt numbers, and the skin frictions (along x and z axis) are defined by [79]:

$$Sh(Re_x)^{-1/2} = -\phi(0)', \tag{21}$$

$$Nu(Re_x)^{-1/2} = -\left(1 + \frac{1}{Rd}\theta_{(w)}(0)^3\right)\theta(0)', \tag{22}$$

$$C_{fx}(Re_x)^{1/2} = \frac{f''(0)}{2}\left(2 + We(n-1)(f''(0))^2\right), \tag{23}$$

$$C_{fz}(Re_x)^{1/2} = \frac{g'(0)}{2}\left(2 + (n-1)We(g'(0))^2\right), \tag{24}$$

where $Re_x = \frac{xu_w}{\nu}$ represents the Reynolds number.

3. Results and Discussion

The homotopy analysis method (HAM) is an analytical procedure which is employed for solving the nonlinear coupled DEs. From its introduction in 1992 [80], HAM has been heavily used by investigators for solving the nonlinear coupled ODEs. The wide range of uses and applications of HAM are because of its convergence properties and initial guess wide range [71,81,82]. The procedure that HAM follows is based on the transformation $\tilde{\Psi} : \hat{X} \times [0,1] \to \hat{Y}$, where $\hat{X}$ and $\hat{Y}$ are the topological spaces. The linear operators are defined as follow:

$$L_{\hat{f}}(\hat{f}) = \hat{f}''', \; L_{\hat{g}}(\hat{g}) = \hat{g}'', \; L_{\hat{\theta}}(\hat{\theta}) = \hat{\theta}'', \text{ and } L_{\hat{\phi}}(\hat{\phi}) = \hat{\phi}''. \tag{25}$$

We have employed HAM in this study for solving Equations (15)–(19). The achieved results are depicted through different graphs and the effects of related parameters over the Carreau fluid hydromagnetic behavior are investigated and explained in detail. Furthermore, the present study results are compared with the published work and the agreement ascertains the accuracy of HAM.

The dependence of $f'(\eta)$ (gradient in the velocity x-component) and $g(\eta)$ (velocity y-component) on augmenting magnetic parameter M are respectively depicted in Figure 2a,b. The values of M used in this Figure are $= 0.5, 1.0, 1.5, 2.0$. It is clear from Figure 2a, that at fixed M, $f'(\eta)$ declines with the rising η. The decline in $f'(\eta)$ is much faster at smaller η values. Furthermore, the increasing magnetic parameter M values result in a downfall in the $f'(\eta)$ profile. It is obvious from the Figure 2a that reduction in the $f'(\eta)$ profile is more visible in the range $\eta = 0.4$ to $\eta = 2.6$. The downfall in the $f'(\eta)$ profile may be associated with the augmenting Lorentz forces due to the enhancing M, which causes to reduce the non-uniformity in the fluid velocity. Figure 2b shows that the velocity $g(\eta)$ changes inversely with the rising η at fixed M. The velocity field augments with the enhancing M. The enhancing behavior of $g(\eta)$ with uplifting M is more dominant upto $\eta = 2.6$. Thus, the augmenting Lorentz forces due to rising M accelerate the fluid flow.

The impact of the Hall parameter (m) on the velocity gradient $f'(\eta)$ and velocity $g(\eta)$ is displayed respectively in Figure 3a,b. The different values of m used in this computation are $0.5, 1.0, 1.5, 2.0$. It is evident from Figure 3a, that initially $f'(\eta)$ augments and then drops with the increasing η values at fixed Hall parameter value. It is further observed that the enhancing m results in the increase of the $f'(\eta)$ profile. The enhancing behavior of $f'(\eta)$ is more apparent from $\eta = 0.4$ to $\eta = 2.4$. The variation of the velocity $g(\eta)$ with enhancing m is displayed in Figure 3b. It can be seen from this figure that at smaller m, the velocity drops with augmenting η. As the value of m is increased to $m = 1.5$ and $m = 2.0$, the trend in the $g(\eta)$ profiles changes. Now initially the velocity increases, reaches to a maximum, and then declines with the increasing η. The variation in the velocity profiles is more dominant at smaller η as can be seen from the figure. The increasing trend with the

augmenting m is due to the higher Hall potentials produced in the fluid which augment the fluid velocity as well as the gradient in the velocity.

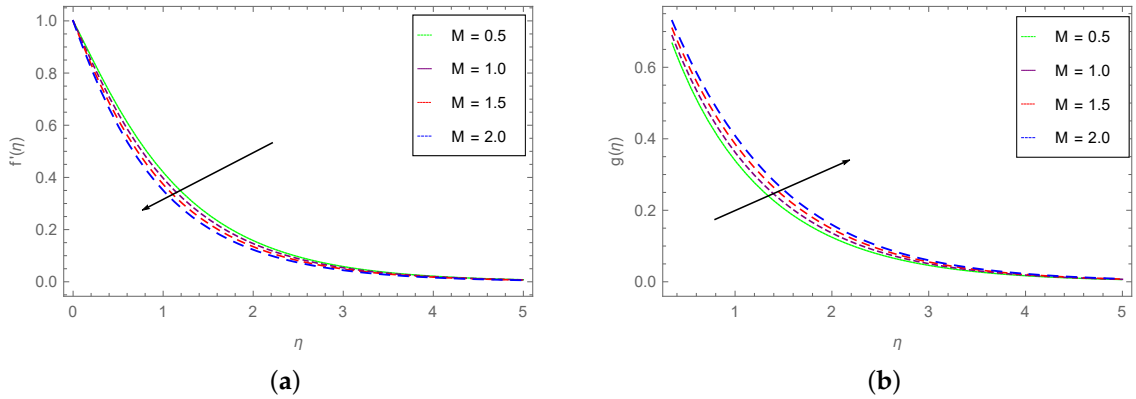

(a) **(b)**

Figure 2. (**a**) $f^{'}(\eta)$ variation with M, and (**b**) $g(\eta)$ dependence on M.

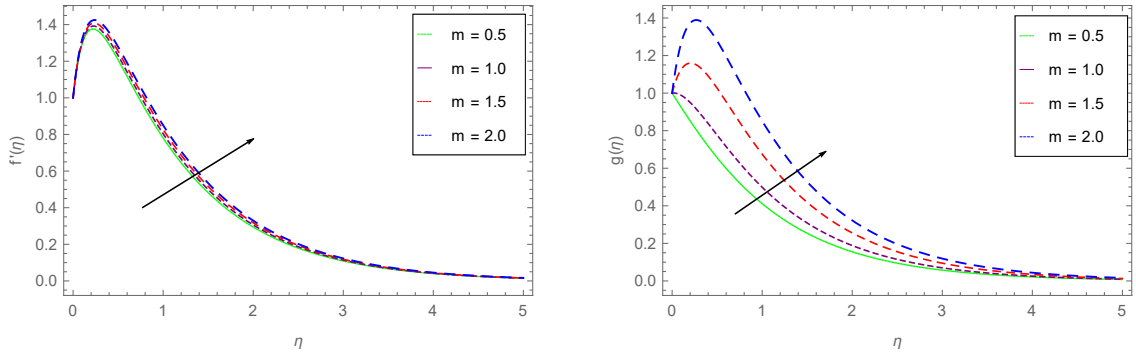

(a) **(b)**

Figure 3. (**a**) $f^{'}(\eta)$ dependence on m and (**b**) $g(\eta)$ variation with m.

Figure 4a,b show the variations of $f^{'}(\eta)$ and $g(\eta)$ with varying Weissenberg number (We). The values of We used in the present computation are $0.30, 0.50, 0.70, 0.90$. From these two figures, it is observed that both $f^{'}(\eta)$ and $g(\eta)$ display almost similar decreasing trend with the increasing We. Thus, it is clear that the enhancing viscous nature of the Carreau fluid associated with the rising We constricts the fluid flow and hence reduces the fluid velocity.

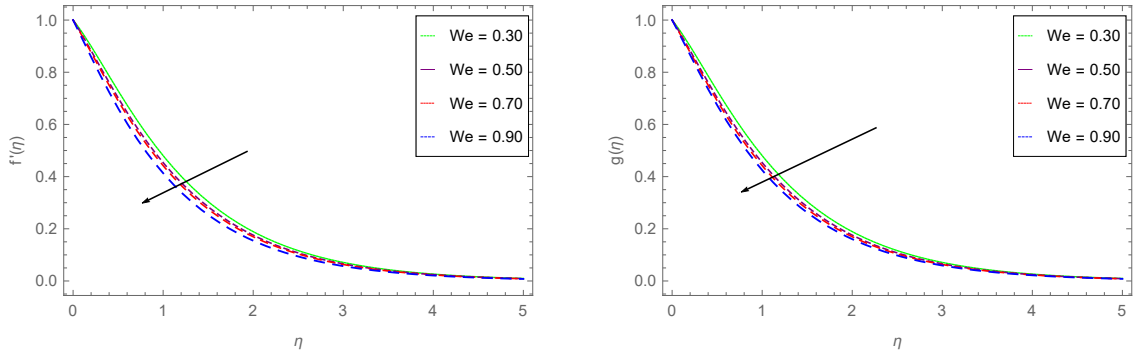

(a) **(b)**

Figure 4. (**a**) $f^{'}(\eta)$ dependence on We and (**b**) $g(\eta)$ dependence on We.

The variation of $f^{'}(\eta)$ with shrinking parameter (ϱ) and the index of power law (n) is depicted respectively in the Figure 5a,b. The values of ϱ used are $4.0, 5.0, 6.0, 7.0$, while those of n are $1.6, 2.2, 2.5, 2.8$. It is observed from Figure 5a that at fixed ϱ, $f^{'}(\eta)$ first drops, reaches to minimum and then enhances with increasing η. Similarly, the $f^{'}(\eta)$ profiles first drop and then augment with enhancing ϱ. Thus, due to suction ($\varrho > 0$) during the Carreau fluid flow, the $f^{'}(\eta)$ profiles rise beyond $\eta = 1$. Beyond $\eta = 3.8$, all the curves for different ϱ overlap with one another. Figure 5b shows the variation of $f^{'}(\eta)$ with changing values of the power law index n. The Figure shows that, at fixed n, $f^{'}(\eta)$ augments with higher η values. The rate of enhancement in $f^{'}(\eta)$ is larger for lower η values in comparison with larger η. By enhancing the values of n, the $f^{'}(\eta)$ profiles drop. The spacing between $f^{'}(\eta)$ curves at different n increases with rising η as clear from the Figure.

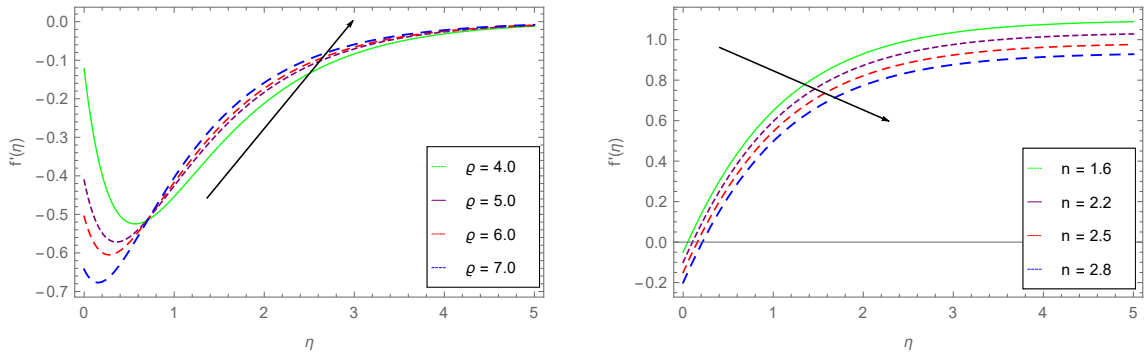

(**a**) (**b**)

Figure 5. (**a**) $f^{'}(\eta)$ dependence on ϱ and (**b**) dependence of $f^{'}(\eta)$ on n.

The variation in $f^{'}(\eta)$ and $\phi(\eta)$ (fluid concentration) with the enhancing values of χ_1 are displayed respectively in Figure 6a,b. The different values of χ_1 used are $\chi_1 = 0.25, 0.50, 0.75, 0.95$. From Figure 6a, it is observed that at a given χ_1, $f^{'}(\eta)$ changes inversely with η. The rate of decline of $f^{'}(\eta)$ is faster at lower η in comparison with larger η values. Furthermore, by augmenting the values of χ_1, the $f^{'}(\eta)$ profiles drop to smaller values. The spacing between the curves for different χ_1 reduces with larger values of χ_1. The different curves overlap beyond $\eta = 4.0$. The concentration field ($\phi(\eta)$) variation with changing χ_1 is depicted in Figure 6b. It can be seen that at fixed χ_1, the concentration field drops with enhancing η. The rate of decline of $\phi(\eta)$ is much larger at smaller η values. An enhancement in the $\phi(\eta)$ profiles is observed with the rising χ_1. The rate of enhancement of $\phi(\eta)$ is larger for the larger χ_1. The $\phi(\eta)$ curves for different χ_1 overlap with one another beyond $\eta = 3.6$.

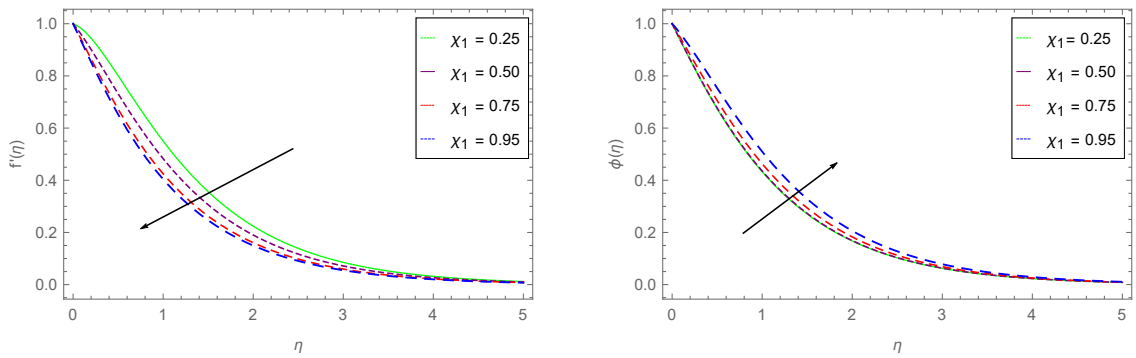

(**a**) (**b**)

Figure 6. (**a**) $f^{'}(\eta)$ variation with χ_1 and (**b**) dependence of $\phi(\eta)$ on χ_1.

The variation of the fluid temperature $\theta(\eta)$ with increasing Pr (Prandtl number) and Rd (radiation parameter) is displayed in Figure 7a,b. The values of Pr are taken as $7.0, 10.0, 13.0, 16.0$, while those of Rd are taken as $1.0, 2.0, 2.5, 3.0$. Figure 7a shows that the Carreau fluid temperature drops with the rising η at fixed Pr. The rate of decrease of $\theta(\eta)$ is much faster at smaller η. As the Pr values are increased, the temperature field profiles drop. The spacing between $\theta(\eta)$ curves is more prominent at the intermediate values of η. The drop in the fluid temperature with the enhancing Prandtl number is due to the smaller thermal diffusivity of the Carreua fluid, which causes a reduction in the temperature of the fluid. Figure 7b depicts the dependence of the temperature field on Rd. It can be observed that the fluid temperature augments with the rising Rd values. The rate of enhancement in $\theta(\eta)$ with increasing Rd is more drastic for smaller η values. The $\theta(\eta)$ curves overlap beyond $\eta = 4.0$. The augmenting fluid temperature with the higher Rd is due to the stronger heat source.

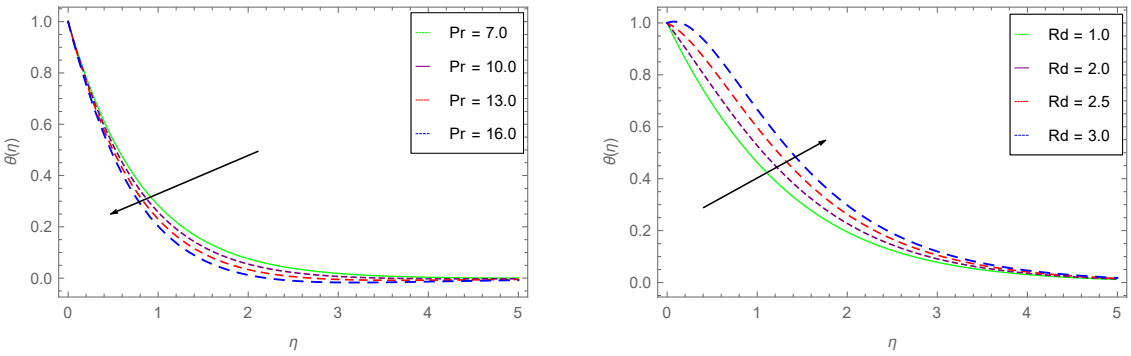

(**a**) (**b**)

Figure 7. (**a**) $\theta(\eta)$ dependence on Pr and (**b**) $\theta(\eta)$ dependence on Rd.

The influence of augmenting values of Weissenberg number (We) and Dufour number (Du) on $\theta(\eta)$ is displayed respectively in Figure 8a,b. The We and Du values are taken as $0.3, 0.5, 0.7, 0.9$ and $0.25, 0.45, 0.65, 0.95$, respectively. It is clear that $\theta(\eta)$ declines with the augmenting η at constant We. The temperature field profiles of the fluid upsurge with the enhancing We values. This means that the augmenting viscous nature of the Carreau fluid associated with the rising We enhances the fluid temperature. The different $\theta(\eta)$ curves overlap beyond $\eta = 4.0$. Figure 8b displays the variation of the Carreau fluid temperature with the enhancing Du (Dufour number). It is observed that the fluid temperature profiles rise with the enhancing Du values. Thus, the accumulation of the fluid particles due to increasing Du raises the fluid temperature.

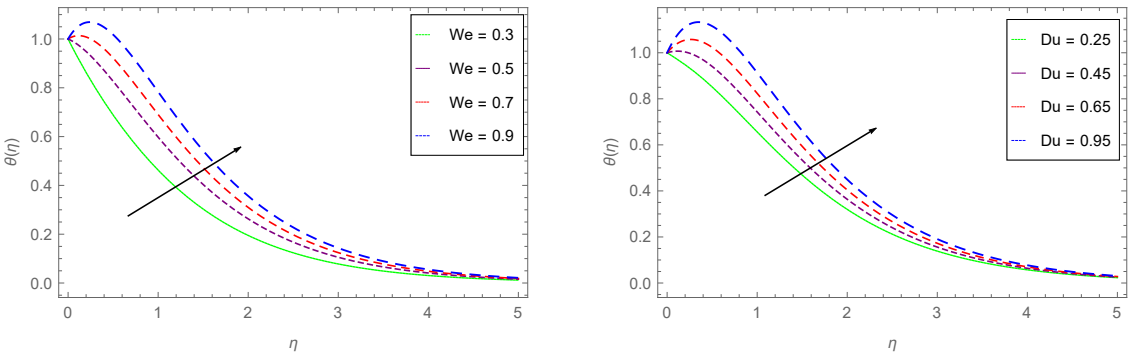

(**a**) (**b**)

Figure 8. (**a**) $\theta(\eta)$ dependence on We and (**b**) $\theta(\eta)$ dependence on Du.

Figure 9a depicts the fluid concentration $\phi(\eta)$ with varying Schmidt number (Sc). From this Figure, we can observe that $\phi(\eta)$ changes inversely with rising η at constant Sc. As Sc changes from 0.10 to 0.40, 0.70, and 0.90, a decreasing behavior in the $\theta(\eta)$ profiles is seen. The different curves overlap beyond $\eta = 3.6$. The higher value of Sc is analogous to smaller value of mass diffusivity, that causes the concentration of the Carreau fluid to drop as can be seen from the Figure. The dependence of $\phi(\eta)$ on the increasing Sr (Soret number) is plotted in Figure 9b. The fluid concentration declines with augmenting η at fixed Sr. An increase is observed in the fluid concentration with the enhancing Sr. As Sr is related with the Carreau fluid temperature gradient, hence, higher Sr denotes greater temperature difference, which causes an enhancement in the concentration.

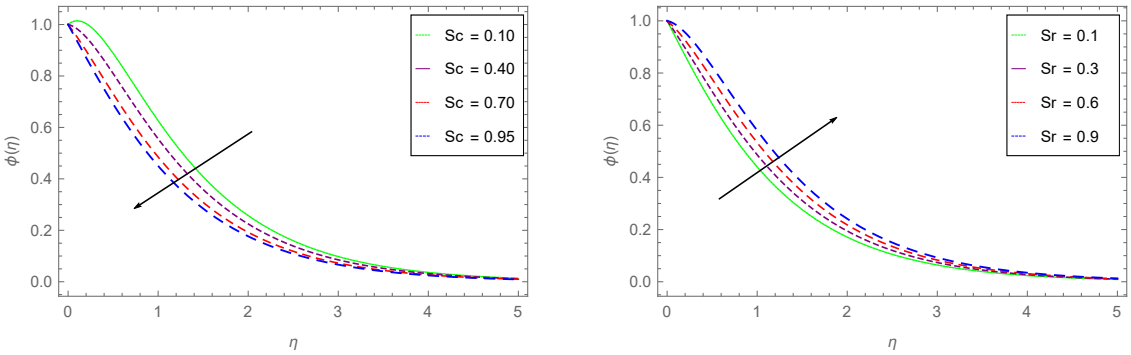

Figure 9. (**a**) $\phi(\eta)$ dependence on Sc and (**b**) dependence of $\phi(\eta)$ on Sr.

4. Tables' Discussion

This section is devoted to comparing the results of this study to the work published and the computation of various quantities of engineering interest with the changing values of the associated parameters. The comparison is carried out in Tables 1–3. The quantities of engineering interest are computed in Tables 4 and 5. The comparison is made with the research work already carried out in ref. [75] as in the following:

The comparison of the skin friction values with varying ϱ and We is shown in Table 1. The Rd, Sr, Du, M, and Sc values are taken as 0. We see complete agreement between the results of our work and the already published work.

Table 1. Computation of C_{fx} for changing ϱ and We, for $Rd = Sr = M = Du = Sc = 0$.

ϱ	We	Reference [75]	Present Results
0.0	0.4	0.9913393	0.99133929
0.3	0.4	1.157602	1.1576019
0.6	0.4	1.348724	1.3487236
0.6	0.0	1.344032	1.3440315
0.6	0.2	1.348725	1.3487250
0.6	0.4	1.333041	1.3330407

Table 2 shows the comparison of Nusselt number (Nu_x) for the varying We, n, ϱ, and Pr, whereas Rd, Sr, Du, M, and Sc are taken as 0. The value of χ_1 is taken as 0.2. Again both results are in tremendous agreement.

Table 2. Computation of Nu_x, when $Rd = Sr = M = Sc = Du = 0$.

We	n	ϱ	Pr	χ_1	Reference [75]	Present Results
0.0	0.6	0.6	0.2	0.2	0.1668374	0.16683740
0.1	0.6	0.6	0.2	0.2	0.1666775	0.16667749
0.2	0.6	0.6	0.2	0.2	0.4741203	0.47412033
0.2	0.3	0.7	1.3	0.2	0.1666314	0.16663136
0.2	0.5	0.7	1.3	0.2	0.1666914	0.16669144
0.2	0.7	0.7	1.3	0.2	0.1667505	0.16675047

Table 3 compares the present and published results for Sh_x (local Sherwood number) for changing Sr. We used $Du = We = 0$. The values of the parameters n, Rd, Pr, and M are kept fixed in computing the values of Sh_x. The comparison proves that both computations are in agreement with each other.

Table 3. Computation of Sh_x, for $Du = We = 0$.

Sr	n	Rd	Pr	M	Reference [75]	Present Results
0.5	0.6	0.5	0.75	0.75	1.2110832	1.21108321
1.0	0.6	0.5	0.75	0.75	1.0581235	1.058124
1.5	0.6	0.5	0.75	0.75	0.905314	0.9053143
2.0	0.6	0.5	0.75	0.75	0.752515	0.7525148

The computation of C_{fx} and C_{fz} with the changing values of M, m, χ_1, and We for suction case is tabulated in Table 4. It is found that C_{fx} first reduces and then increases with rising magnetic parameter (M). The skin friction C_{fx} drops with the augmenting values of m, χ_1 and We. The other skin friction component C_{fz} augments (drops) with the rising values of M, χ_1 and We (m).

Table 4. Computation of C_{fx} and C_{fz} in the suction case.

M	m	χ_1	We	$Re_x^{\frac{1}{2}} C_{fx}$	$Re_x^{\frac{1}{2}} C_{fz}$
0.5	0.5	0.25	0.30	−1.27682794	0.02280230
1	–	–	–	−1.47275352	0.03841483
1.5	–	–	–	−1.52006594	0.04188107
2	–	–	–	−1.24036061	0.09561891
–	1	–	–	−1.17768683	0.12810091
–	1.5	–	–	−1.30688120	0.02219887
–	2	–	–	−1.33663381	0.02161783
–	–	0.50	–	−1.29858315	0.02300640
–	–	0.75	–	−1.31813402	0.02318486
–	–	0.95	–	−1.32674352	0.02452684
–	–	–	0.50	−1.38932465	0.02918536
–	–	–	0.70	−1.40374526	0.03326478
–	–	–	0.90	−1.40374537	0.03326589

The variation of Nu_x and Sh_x with the augmenting M, n, Sr, Du, Rd, and χ_1 in the blowing case is shown in Table 5. It is clear that both Nu_x and Sh_x drop and then enhance with enhancing M. The Nusselt number first increases and then decreases, whereas the Sherwood number enhances with the higher n. Furthermore the Nusselt number enhances with the augmenting values of all the remaining parameters, that is Sr, Du, Rd and χ_1. The Sherwood number rises (declines) with the increasing values of Du and Rd (Sr and χ_1).

Table 5. Nu_x, and Sh_x in the case of blowing.

M	n	Sr	Du	Rd	χ_1	$Nu/Re_x^{\frac{-1}{2}}$	$Sh/Re_x^{\frac{-1}{2}}$
0.5	1.6	0.1	0.25	1	0.25	0.114028	0.139181
1	–	–	–	–	–	0.106677	0.134409
1.5	–	–	–	–	–	0.100334	0.130193
2	1	–	–	–	–	0.106198	0.134071
–	2.2	–	–	–	–	0.109861	0.136627
–	2.5	–	–	–	–	0.113931	0.139391
–	2.8	0.2	–	–	–	0.113041	0.142802
–	–	0.4	–	–	–	0.108654	0.137044
–	–	0.6	–	–	–	0.104832	0.131925
–	–	–	0.2	–	–	0.125738	0.130361
–	–	–	0.4	–	–	0.112658	0.133111
–	–	–	0.6	–	–	0.101036	0.135657
–	–	–	–	0.5	–	0.111641	0.133395
–	–	–	–	1.0	–	0.106677	0.134407
–	–	–	–	1.5	–	0.102281	0.135322
–	–	–	–	–	0.1	0.110879	0.137607
–	–	–	–	–	0.3	0.102933	0.131509
–	–	–	–	–	0.5	0.096511	0.126388

5. Conclusions

This section concludes the main findings of the present research work. The investigation of mass and thermal energy transfer of the 3D Carreau fluid moving through a permeable and stretching (shrinking) sheet is undertaken by considering the effects of thermal radiations, cross diffusion, and Hall current. Suitable similarity relations are employed in order to transform the set of coupled PDEs to a system of coupled ODEs. The set of coupled ODEs is then solved through the well-known standard analytical technique of HAM. The influence of the relevant physical variables on the hydromagnetic behavior of the Carreau fluid 3D flow is examined through various plots. The variations of the coefficients of skin friction, local Nusselt, and Sherwood numbers with the changing parameter values are shown through various tables. The important findings of this work are outlined as below:

- The gradient in velocity $f^{'}(\eta)$ reduces with the augmenting M, We, and χ_1, whereas it enhances with the Hall parameter (m) and the shrinking parameter (ϱ).
- The velocity component $g(\eta)$ enhances with augmenting M, m, while it declines with Wesinberg number (We).
- The Carreau fluid temperature enhances with the rising Rd, We, and Du, while it reduces with the increasing Pr (Prandtl number) values.
- The concentration of the fluid augments with enhancing χ_1 while it reduces with the augmenting Sc values.
- The skin friction coefficients (C_{fx}) drops with the enhancing m, χ_1, and We. The other component (C_{fz}) enhances with the rising M, χ_1, and We.
- The local Nusselt number depreciates with the enhancing Sr, Du, Rd, and χ_1, while the Sherwood number increases (depreciates) with the rising n, Du, and Rd (Sr and χ_1).
- The published and obtained results show an agreement which validates the employed analytical procedure accuracy.

Author Contributions: Conceptualization, A.U., I., and M.M.S.; software, S.K., A.U., and M.A.; writing—original draft preparation, I., M.M.S., and T.A.; writing—review and editing, A.K., T.A., S.K., and W.K.M.; formal analysis, W.K.M., I., and M.A.; validation, I., S.K., and A.U.; methodology, A.U., T.A., M.A., and W.K.M.; investigation, W.K.M., A.K., and S.K.; resources, M.M.S., A.K., and S.K.; project administration, M.M.S., M.A., and W.K.M.; funding acquisition, A.K. and T.A. All authors have read and agreed to the published version of the manuscript.

Funding: This research received no external funding.

Institutional Review Board Statement: Not applicable.

Informed Consent Statement: Not applicable.

Data Availability Statement: The data used to support the findings of this study are available from the corresponding author upon request.

Acknowledgments: Aziz Khan and Thabet Abdeljawad acknowledge the support provided by Prince Sultan University for funding this work through research group Nonlinear Analysis Methods in Applied Mathematics (NAMAM)group number RG-DES-2017–01-17.

Conflicts of Interest: The authors declare no conflict of interest.

Abbreviations

The below mentioned parameters and abbreviations with their possible dimensions are used in this article:

σ	Electrical conductivity $\frac{\mathrm{S}}{\mathrm{m}}$
B_0	magnetic field strength T
Re_x	Local Reynolds number
C_{fx}	Local Skin friction
m	Hall parameter $\frac{\mathrm{m}^3}{\mathrm{C}}$
ϱ	Suction/ injection parameter
J_w	Mass flux $(\frac{\mathrm{kg}}{\mathrm{s\,m}^2})$
f	Dimensionless velocity
ϕ	Dimensionless concentration
θ	Dimensionless temperature
∞	Condition at infinity
x, y, and z	Coordinates (m)
0	Reference condition
η	Similarity variable
Sc	Schmidt number
γ	Thermal relaxation parameter
Du	Dufour number
u_w	Stretching velocity $(\frac{\mathrm{m}}{\mathrm{s}})$
Pr	Prandtl number
T	Fluid temperature (K)
ρ	Density $(\frac{\mathrm{kg}}{\mathrm{m}^3})$
v	Kinematic viscosity $\frac{\mathrm{m}^2}{\mathrm{s}}$
μ	Dynamic viscosity mPa
t	Time (s)
C_p	Specific heat $(\frac{\mathrm{J}}{\mathrm{kg\,K}})$
n	Power law index
k_T	Thermal diffusion ratio
L_1	Velocity slip factor
h_2	Convective mass transfer coefficient
h_1	Convective heat transfer coefficient
τ	Extra stress tensor
M	Magnetic field interaction parameter
Π	Strain rate tensor
σ^*	Stefan Boltzmann constant
χ_1	Velocity slip parameter
χ_2	Thermal profile slip parameter
χ_3	Concentration profile slip parameter
We	Weissenberg number

References

1. Moradikazerouni, A.; Afrand, M.; Alsarraf, J.; Mahian, O.; Wongwises, S.; Tran, M.D. Comparison of the effect of five different entrance channel shapes of a micro-channel heat sink in forced convection with application to cooling a supercomputer circuit board. *Appl. Therm. Eng.* **2019**, *150*, 1078–1089. [CrossRef]
2. Moradikazerouni, A.; Afrand, M.; Alsarraf, J.; Wongwises, S.; Asadi, A.; Nguyen, T.K. Investigation of a computer CPU heat sink under laminar forced convection using a structural stability method. *Int. J. Heat Mass Transf.* **2019**, *134*, 1218–1226. [CrossRef]
3. Crane, L.J. Flow past a stretching plate. *Z. Angew. Math. Phys. ZAMP* **1970**, *21*, 645–647. [CrossRef]
4. Eid, M.R.; Mahny, K.L. Flow and heat transfer in a porous medium saturated with a Sisko nanofluid over a nonlinearly stretching sheet with heat generation/absorption. *Heat Transf. Asian Res.* **2018**, *47*, 54–71. [CrossRef]
5. Vajravelu, K. Viscous flow over a nonlinearly stretching sheet. *Appl. Math. Comput.* **2001**, *124*, 281–288. [CrossRef]
6. Liu, I.C.; Wang, H.H.; Peng, Y.F. Flow and heat transfer for three-dimensional flow over an exponentially stretching surface. *Chem. Eng. Commun.* **2013**, *200*, 253–268. [CrossRef]
7. Hayat, T.; Asad, S.; Mustafa, M.; Alsaedi, A. Boundary layer flow of Carreau fluid over a convectively heated stretching sheet. *Appl. Math. Comput.* **2014**, *246*, 12–22. [CrossRef]
8. Schlichting, H.; Gersten, K. *Boundary-Layer Theory*; Springer: Berlin/Heidelberg, Germany, 2016.
9. Dash, G.; Tripathy, R.; Rashidi, M.; Mishra, S. Numerical approach to boundary layer stagnation-point flow past a stretching/shrinking sheet. *J. Mol. Liq.* **2016**, *221*, 860–866. [CrossRef]
10. Ajlouni, A.W.M.; Al-Rabai'ah, H.A. Fractional-calculus diffusion equation. *Nonlinear Biomed. Phys.* **2010**, *4*, 3. [CrossRef] [PubMed]
11. Ishak, A.; Nazar, R.; Pop, I. Hydromagnetic flow and heat transfer adjacent to a stretching vertical sheet. *Heat Mass Transf.* **2008**, *44*, 921. [CrossRef]
12. Xu, H.; Liao, S.J.; Pop, I. Series solutions of unsteady three-dimensional MHD flow and heat transfer in the boundary layer over an impulsively stretching plate. *Eur. J. Mech. B/Fluids* **2007**, *26*, 15–27. [CrossRef]
13. Ishak, A.; Jafar, K.; Nazar, R.; Pop, I. MHD stagnation point flow towards a stretching sheet. *Phys. A Stat. Mech. Its Appl.* **2009**, *388*, 3377–3383. [CrossRef]
14. Naganthran, K.; Nazar, R.; Pop, I. A study on non-Newtonian transport phenomena in a mixed convection stagnation point flow with numerical simulation and stability analysis. *Eur. Phys. J. Plus* **2019**, *134*, 1–14. [CrossRef]
15. Naganthran, K.; Nazar, R.; Pop, I. Stability analysis of impinging oblique stagnation-point flow over a permeable shrinking surface in a viscoelastic fluid. *Int. J. Mech. Sci.* **2017**, *131*, 663–671. [CrossRef]
16. Vajravelu, K.; Hadjinicolaou, A. Convective heat transfer in an electrically conducting fluid at a stretching surface with uniform free stream. *Int. J. Eng. Sci.* **1997**, *35*, 1237–1244. [CrossRef]
17. Pop, I.; Na, T.Y. A note on MHD flow over a stretching permeable surface. *Mech. Res. Commun.* **1998**, *25*, 263–269. [CrossRef]
18. Freidoonimehr, N.; Rashidi, M.M.; Mahmud, S. Unsteady MHD free convective flow past a permeable stretching vertical surface in a nano-fluid. *Int. J. Therm. Sci.* **2015**, *87*, 136–145. [CrossRef]
19. Ahmad, H.; Seadawy, A.R.; Khan, T.A.; Thounthong, P. Analytic approximate solutions for some nonlinear Parabolic dynamical wave equations. *J. Taibah Univ. Sci.* **2020**, *14*, 346–358. [CrossRef]
20. Jamaludin, A.; Naganthran, K.; Nazar, R.; Pop, I. Thermal radiation and MHD effects in the mixed convection flow of Fe3O4–water ferrofluid towards a nonlinearly moving surface. *Processes* **2020**, *8*, 95. [CrossRef]
21. Lund, L.A.; Omar, Z.; Khan, I.; Baleanu, D.; Nisar, K.S. Dual similarity solutions of MHD stagnation point flow of Casson fluid with effect of thermal radiation and viscous dissipation: Stability analysis. *Sci. Rep.* **2020**, *10*, 1–13. [CrossRef] [PubMed]
22. Reddy, M.G. Influence of magnetohydrodynamic and thermal radiation boundary layer flow of a nanofluid past a stretching sheet. *J. Sci. Res.* **2014**, *6*, 257–272. [CrossRef]
23. Gnaneswara Reddy, M. Thermal radiation and chemical reaction effects on MHD mixed convective boundary layer slip flow in a porous medium with heat source and Ohmic heating. *EPJP* **2014**, *129*, 41. [CrossRef]
24. AboEldahab, E.M. Radiation effect on heat transfer in an electrically conducting fluid at a stretching surface with a uniform free stream. *J. Phys. D Appl. Phys.* **2000**, *33*, 3180. [CrossRef]
25. Abo-Eldahab, E.M.; El Gendy, M.S. Radiation effect on convective heat transfer in an electrically conducting fluid at a stretching surface with variable viscosity and uniform free stream. *Phys. Scr.* **2000**, *62*, 321. [CrossRef]
26. Reddy, M.G. Effects of Thermophoresis, Viscous Dissipation and Joule Heating on Steady MHD Flow over an Inclined Radiative Isothermal Permeable Surface with Variable Thermal Conductivity. *J. Appl. Fluid Mech.* **2014**, *7*, 51–61.
27. Anwar, T.; Kumam, P.; Khan, I.; Thounthong, P. Generalized Unsteady MHD Natural Convective Flow of Jeffery Model with ramped wall velocity and Newtonian heating; A Caputo-Fabrizio Approach. *Chin. J. Phys.* **2020**, *68*, 849–865. [CrossRef]
28. Fayz-Al-Asad, M.; Alam, M.N.; Ahmad, H.; Sarker, M.; Alsulami, M.; Gepreel, K.A. Impact of a closed space rectangular heat source on natural convective flow through triangular cavity. *Results Phys.* **2021**, *23*, 104011. [CrossRef]
29. Anwar, T.; Kumam, P.; Baleanu, D.; Khan, I.; Thounthong, P. Radiative heat transfer enhancement in MHD porous channel flow of an Oldroyd-B fluid under generalized boundary conditions. *Phys. Scr.* **2020**, *95*, 115211. [CrossRef]
30. Farooq, A.; Kamran, M.; Bashir, Y.; Ahmad, H.; Shahzad, A.; Chu, Y.M. On the flow of MHD generalized maxwell fluid via porous rectangular duct. *Open Phys.* **2020**, *18*, 989–1002. [CrossRef]

31. Ma, Y.; Shahsavar, A.; Moradi, I.; Rostami, S.; Moradikazerouni, A.; Yarmand, H.; Zulkifli, N.W.B.M. Using finite volume method for simulating the natural convective heat transfer of nano-fluid flow inside an inclined enclosure with conductive walls in the presence of a constant temperature heat source. *Phys. A Stat. Mech. Its Appl.* **2019**, 123035. [CrossRef]
32. Tian, Z.; Rostami, S.; Taherialekouhi, R.; Karimipour, A.; Moradikazerouni, A.; Yarmand, H.; Zulkifli, N.W.B.M. Prediction of rheological behavior of a new hybrid nanofluid consists of copper oxide and multi wall carbon nanotubes suspended in a mixture of water and ethylene glycol using curve-fitting on experimental data. *Phys. A Stat. Mech. Its Appl.* **2020**, *549*, 124101. [CrossRef]
33. Shah, Z.; Islam, S.; Gul, T.; Bonyah, E.; Khan, M.A. The electrical MHD and hall current impact on micropolar nanofluid flow between rotating parallel plates. *Results Phys.* **2018**, *9*, 1201–1214. [CrossRef]
34. Shah, Z.; Islam, S.; Ayaz, H.; Khan, S. Radiative heat and mass transfer analysis of micropolar nanofluid flow of Casson fluid between two rotating parallel plates with effects of Hall current. *J. Heat Transf.* **2019**, *141*, 022401. [CrossRef]
35. Khan, A.; Shah, Z.; Islam, S.; Khan, S.; Khan, W.; Khan, A.Z. Darcy–Forchheimer flow of micropolar nanofluid between two plates in the rotating frame with non-uniform heat generation/absorption. *Adv. Mech. Eng.* **2018**, *10*, 1687814018808850. [CrossRef]
36. Hayat, T.; Rashid, M.; Imtiaz, M.; Alsaedi, A. Magnetohydrodynamic (MHD) flow of Cu-water nanofluid due to a rotating disk with partial slip. *AIP Adv.* **2015**, *5*, 067169. [CrossRef]
37. Vo, D.D.; Alsarraf, J.; Moradikazerouni, A.; Afrand, M.; Salehipour, H.; Qi, C. Numerical investigation of γ-AlOOH nano-fluid convection performance in a wavy channel considering various shapes of nanoadditives. *Powder Technol.* **2019**, *345*, 649–657. [CrossRef]
38. Alsarraf, J.; Moradikazerouni, A.; Shahsavar, A.; Afrand, M.; Salehipour, H.; Tran, M.D. Hydrothermal analysis of turbulent boehmite alumina nanofluid flow with different nanoparticle shapes in a minichannel heat exchanger using two-phase mixture model. *Phys. A Stat. Mech. Its Appl.* **2019**, *520*, 275–288. [CrossRef]
39. Abouelregal, A.E.; Ahmad, H. Thermodynamic modeling of viscoelastic thin rotating microbeam based on non-Fourier heat conduction. *Appl. Math. Model.* **2021**, *91*, 973–988. [CrossRef]
40. Asadi, A.; Aberoumand, S.; Moradikazerouni, A.; Pourfattah, F.; Żyła, G.; Estellé, P.; Mahian, O.; Wongwises, S.; Nguyen, H.M.; Arabkoohsar, A. Recent advances in preparation methods and thermophysical properties of oil-based nanofluids: A state-of-the-art review. *Powder Technol.* **2019**, *352*, 209–226. [CrossRef]
41. Abouelregal, A.E.; Moustapha, M.V.; Nofal, T.A.; Rashid, S.; Ahmad, H. Generalized thermoelasticity based on higher-order memory-dependent derivative with time delay. *Results Phys.* **2021**, *20*, 103705. [CrossRef]
42. Shi, E.; Zang, X.; Jiang, C.; Mohammadpourfard, M. Entropy generation analysis for thermomagnetic convection of paramagnetic fluid inside a porous enclosure in the presence of magnetic quadrupole field. *J. Therm. Anal. Calorim.* **2020**, *139*, 2005–2022. [CrossRef]
43. Soleiman, A.; Abouelregal, A.E.; Ahmad, H.; Thounthong, P. Generalized thermoviscoelastic model with memory dependent derivatives and multi-phase delay for an excited spherical cavity. *Phys. Scr.* **2020**, *95*, 115708. [CrossRef]
44. Alam, M.K.; Memon, K.; Siddiqui, A.; Shah, S.; Farooq, M.; Ayaz, M.; Nofal, T.A.; Ahmad, H. Modeling and analysis of high shear viscoelastic Ellis thin liquid film phenomena. *Phys. Scr.* **2021**, *96*, 055201. [CrossRef]
45. Abouelregal, A.E.; Ahmad, H. Response of thermoviscoelastic microbeams affected by the heating of laser pulse under thermal and magnetic fields. *Phys. Scr.* **2020**, *95*, 125501. [CrossRef]
46. Nisar, K.S.; Khan, U.; Zaib, A.; Khan, I.; Morsy, A. A novel study of radiative flow involving micropolar nanoliquid from a shrinking/stretching curved surface including blood gold nanoparticles. *Eur. Phys. J. Plus* **2020**, *135*, 1–19. [CrossRef]
47. Carreau, P.J. Rheological equations from molecular network theories. *Trans. Soc. Rheol.* **1972**, *16*, 99–127. [CrossRef]
48. Ali, N.; Hayat, T. Peristaltic motion of a Carreau fluid in an asymmetric channel. *Appl. Math. Comput.* **2007**, *193*, 535–552. [CrossRef]
49. Goodarzi, M.; Javid, S.; Sajadifar, A.; Nojoomizadeh, M.; Motaharipour, S.H.; Bach, Q.V.; Karimipour, A. Slip velocity and temperature jump of a non-Newtonian nanofluid, aqueous solution of carboxy-methyl cellulose/aluminum oxide nanoparticles, through a microtube. *Int. J. Numer. Methods Heat Fluid Flow* **2019**, *29*, 1606–1628. [CrossRef]
50. Maleki, H.; Alsarraf, J.; Moghanizadeh, A.; Hajabdollahi, H.; Safaei, M.R. Heat transfer and nanofluid flow over a porous plate with radiation and slip boundary conditions. *J. Cent. South Univ.* **2019**, *26*, 1099–1115. [CrossRef]
51. Hayat, T.; Saleem, N.; Ali, N. Effect of induced magnetic field on peristaltic transport of a Carreau fluid. *Commun. Nonlinear Sci. Numer. Simul.* **2010**, *15*, 2407–2423. [CrossRef]
52. Tshehla, M. The flow of Carreau fluid down an incline with a free surface. *Int. J. Phys. Sci* **2011**, *6*, 3896–3910.
53. Ellahi, R.; Riaz, A.; Nadeem, S.; Ali, M. Peristaltic flow of Carreau fluid in a rectangular duct through a porous medium. *Math. Probl. Eng.* **2012**, *2012*. [CrossRef]
54. Machireddy, G.R.; Polarapu, P.; Bandari, S. Effects of magnetic field and Ohmic heating on viscous flow of a nanofluid towards a nonlinear permeable stretching sheet. *J. Nanofluids* **2016**, *5*, 459–470. [CrossRef]
55. Jiaqiang, E.; Jin, Y.; Deng, Y.; Zuo, W.; Zhao, X.; Han, D.; Peng, Q.; Zhang, Z. Wetting models and working mechanisms of typical surfaces existing in nature and their application on superhydrophobic surfaces: A review. *Adv. Mater. Interfaces* **2018**, *5*, 1701052.
56. Tassaddiq, A.; Khan, I.; Nisar, K.S.; Singh, J. MHD flow of a generalized Casson fluid with Newtonian heating: A fractional model with Mittag–Leffler memory. *Alex. Eng. J.* **2020**, *59*, 3049–3059. [CrossRef]
57. Khan, Z.A.; Haq, S.U.; Khan, T.S.; Khan, I.; Nisar, K.S. Fractional Brinkman type fluid in channel under the effect of MHD with Caputo-Fabrizio fractional derivative. *Alex. Eng. J.* **2020**, *59*, 2901–2910. [CrossRef]

58. Krisna, P.M.; Sandeep, N.; Sugunamma, V. Effects of radiation and chemical reaction on MHD convective flow over a permeable stretching surface with suction and heat generation. *Walailak J. Sci. Technol. (WJST)* **2015**, *12*, 831–847.
59. Sandeep, N.; Sulochana, C.; Sugunamma, V. Radiation and magnetic field effects on unsteady mixed convection flow over a vertical stretching/shrinking surface with suction/injection. *Ind. Eng. Lett.* **2015**, *5*, 127–136.
60. Jonnadula, M.; Polarapu, P.; Reddy, G. Influence of thermal radiation and chemical reaction on MHD flow, heat and mass transfer over a stretching surface. *Procedia Eng.* **2015**, *127*, 1315–1322. [CrossRef]
61. Maleki, H.; Safaei, M.R.; Togun, H.; Dahari, M. Heat transfer and fluid flow of pseudo-plastic nanofluid over a moving permeable plate with viscous dissipation and heat absorption/generation. *J. Therm. Anal. Calorim.* **2019**, *135*, 1643–1654. [CrossRef]
62. Gheynani, A.R.; Akbari, O.A.; Zarringhalam, M.; Shabani, G.A.S.; Alnaqi, A.A.; Goodarzi, M.; Toghraie, D. Investigating the effect of nanoparticles diameter on turbulent flow and heat transfer properties of non-Newtonian carboxymethyl cellulose/CuO fluid in a microtube. *Int. J. Numer. Methods Heat Fluid Flow* **2019**, *29*, 1699–1723. [CrossRef]
63. Maleki, H.; Safaei, M.R.; Alrashed, A.A.; Kasaeian, A. Flow and heat transfer in non-Newtonian nanofluids over porous surfaces. *J. Therm. Anal. Calorim.* **2019**, *135*, 1655–1666. [CrossRef]
64. Nazari, S.; Ellahi, R.; Sarafraz, M.; Safaei, M.R.; Asgari, A.; Akbari, O.A. Numerical study on mixed convection of a non-Newtonian nanofluid with porous media in a two lid-driven square cavity. *J. Therm. Anal. Calorim.* **2020**, *140*, 1121–1145. [CrossRef]
65. Biswal, S.; Sahoo, P. Hall effect on oscillatory hydromagnetic free convective flow of a visco-elastic fluid past an infinite vertical porous flat plate with mass transfer. *Proc. Natl. Acad. Sci. India Sect. A* **1999**, *1, 45–58*.
66. Changal, R.M.; Ananda, R.N.; Vijaya, K.V.S. Hall-current effects on unsteady MHD flow between stretching sheet and an oscillating porous upper parallel plate with constant suction. *Therm. Sci.* **2011**, *15*, 527–536. [CrossRef]
67. Datta, N.; Jana, R.N. Oscillatory magnetohydrodynamic flow past a flat plate with Hall effects. *J. Phys. Soc. Jpn.* **1976**, *40*, 1469–1474. [CrossRef]
68. Aboeldahab, E.M.; Elbarbary, E.M. Hall current effect on magnetohydrodynamic free-convection flow past a semi-infinite vertical plate with mass transfer. *Int. J. Eng. Sci.* **2001**, *39*, 1641–1652. [CrossRef]
69. Khan, I.; Memon, A.A.; Memon, M.A.; Bhatti, K.; Shaikh, G.M.; Baleanu, D.; Alhussain, Z.A. Finite Element Least Square Technique for Newtonian Fluid Flow through a Semicircular Cylinder of Recirculating Region via COMSOL Multiphysics. *J. Math.* **2020**, *2020*. [CrossRef]
70. Rajput, U.; Kanaujia, N. Chemical reaction in MHD flow past a vertical plate with mass diffusion and constant wall temperature with hall current. *Int. J. Eng. Sci. Technol.* **2016**, *8*, 28–38. [CrossRef]
71. Shah, Z.; Dawar, A.; Khan, I.; Islam, S.; Ching, D.L.C.; Khan, A.Z. Cattaneo-Christov model for electrical magnetite micropoler Casson ferrofluid over a stretching/shrinking sheet using effective thermal conductivity model. *Case Stud. Therm. Eng.* **2019**, *13*, 100352. [CrossRef]
72. Ullah, A.; Alzahrani, E.O.; Shah, Z.; Ayaz, M.; Islam, S. Nanofluids thin film flow of Reiner-Philippoff fluid over an unstable stretching surface with Brownian motion and thermophoresis effects. *Coatings* **2019**, *9*, 21. [CrossRef]
73. Alharbi, S.O.; Dawar, A.; Shah, Z.; Khan, W.; Idrees, M.; Islam, S.; Khan, I. Entropy generation in MHD eyring–powell fluid flow over an unsteady oscillatory porous stretching surface under the impact of thermal radiation and heat source/sink. *Appl. Sci.* **2018**, *8*, 2588. [CrossRef]
74. Hayat, T.; Ahmed, B.; Abbasi, F.; Alsaedi, A. Numerical investigation for peristaltic flow of Carreau–Yasuda magneto-nanofluid with modified Darcy and radiation. *J. Therm. Anal. Calorim.* **2019**, *137*, 1359–1367. [CrossRef]
75. Ullah, A.; Hafeez, A.; Mashwani, W.K.; Kumam, W.; Kumam, P.; Ayaz, M. Non-Linear Thermal Radiations and Mass Transfer Analysis on the Processes of Magnetite Carreau Fluid Flowing Past a Permeable Stretching/Shrinking Surface under Cross Diffusion and Hall Effect. *Coatings* **2020**, *10*, 523. [CrossRef]
76. Carreau, P.; Kee, D.D.; Daroux, M. An analysis of the viscous behaviour of polymeric solutions. *Can. J. Chem. Eng.* **1979**, *57*, 135–140. [CrossRef]
77. Ghadikolaei, S.; Hosseinzadeh, K.; Yassari, M.; Sadeghi, H.; Ganji, D. Analytical and numerical solution of non-Newtonian second-grade fluid flow on a stretching sheet. *Therm. Sci. Eng. Prog.* **2018**, *5*, 309–316. [CrossRef]
78. Vo, D.D.; Shah, Z.; Sheikholeslami, M.; Shafee, A.; Nguyen, T.K. Numerical investigation of MHD nanomaterial convective migration and heat transfer within a sinusoidal porous cavity. *Phys. Scr.* **2019**, *94*, 115225. [CrossRef]
79. Olajuwon, I.B. Convection heat and mass transfer in a hydromagnetic Carreau fluid past a vertical porous plate in presence of thermal radiation and thermal diffusion. *Therm. Sci.* **2011**, *15*, 241–252. [CrossRef]
80. Liao, S.J. The Proposed Homotopy Analysis Technique for the Solution Of Nonlinear problems. Ph.D. Thesis, Shanghai Jiao Tong University Shanghai, Shanghai, China, 1992.
81. Khan, N.S.; Zuhra, S.; Shah, Z.; Bonyah, E.; Khan, W.; Islam, S. Slip flow of Eyring-Powell nanoliquid film containing graphene nanoparticles. *AIP Adv.* **2018**, *8*, 115302. [CrossRef]
82. Sohail, M.; Naz, R.; Shah, Z.; Kumam, P.; Thounthong, P. Exploration of temperature dependent thermophysical characteristics of yield exhibiting non-Newtonian fluid flow under gyrotactic microorganisms. *AIP Adv.* **2019**, *9*, 125016. [CrossRef]